Article

Correlation-Driven Topological Transition in Janus Two-Dimensional Vanadates

Ghulam Hussain [1], Amar Fakhredine [2], Rajibul Islam [1], Raghottam M. Sattigeri [1] [ID], Carmine Autieri [1,*] [ID] and Giuseppe Cuono [1] [ID]

1 International Research Centre MagTop, Institute of Physics, Polish Academy of Sciences, Aleja Lotników 32/46, 02668 Warsaw, Poland
2 Institute of Physics, Polish Academy of Sciences, Aleja Lotników 32/46, 02668 Warsaw, Poland
* Correspondence: autieri@magtop.ifpan.edu.pl

Abstract: The appearance of intrinsic ferromagnetism in 2D materials opens the possibility of investigating the interplay between magnetism and topology. The magnetic anisotropy energy (MAE) describing the easy axis for magnetization in a particular direction is an important yardstick for nanoscale applications. Here, the first-principles approach is used to investigate the electronic band structures, the strain dependence of MAE in pristine VSi_2Z_4 (Z = P, As) and its Janus phase $VSiGeP_2As_2$ and the evolution of the topology as a function of the Coulomb interaction. In the Janus phase the compound presents a breaking of the mirror symmetry, which is equivalent to having an electric field, and the system can be piezoelectric. It is revealed that all three monolayers exhibit ferromagnetic ground state ordering, which is robust even under biaxial strains. A large value of coupling J is obtained, and this, together with the magnetocrystalline anisotropy, will produce a large critical temperature. We found an out-of-plane (in-plane) magnetization for VSi_2P_4 (VSi_2As_4), and an in-plane magnetization for $VSiGeP_2As_2$. Furthermore, we observed a correlation-driven topological transition in the Janus $VSiGeP_2As_2$. Our analysis of these emerging pristine and Janus-phased magnetic semiconductors opens prospects for studying the interplay between magnetism and topology in two-dimensional materials.

Keywords: correlation-driven topological transition; vanadates; density functional theory; 2D ferromagnetism

1. Introduction

Since the observation of intrinsic ferromagnetism in two-dimensional layered materials (2D) such as $CrGeTe_3$ [1] and CrI_3 [2], the fields of magnetism and spintronics have received tremendous research attention in the 2D limit [3–14]. The atomically thin 2D magnetic materials are considered ideal systems, where the magnetic and spin-related features can effectively be controlled and modulated via proximity effects, electric field, magnetic field, strain, defects and optical doping [15–22]. Unlike bulk materials, where magnetic ordering is possible without magnetic anisotropy, long-range magnetic ordering in layered 2D materials is not conceivable in systems deprived of magnetic anisotropy, which is necessary to balance out thermal fluctuations [23]. Due to the fact that magnetic anisotropy is primarily caused by spin-orbit coupling (SOC) effects [24], SOC becomes a crucial characteristic. Furthermore, spintronic devices such as magnetic tunnel junctions and spin valves show enhanced performance based on 2D magnetic structures with substantial magnetic anisotropy [25–27]. It has been demonstrated that strain engineering is an effective method of tuning the magnetic, electronic and optical characteristics of materials [28–33].

The recently discovered new family of 2D layered materials MA_2Z_4, where M, A and Z represent the transition metal atoms (Mo, W, Hf, Cr, V), IV-elements (Si, Ge) and V-elements (N, As, P), respectively [34], has sparked intense interest in different studies [35–44]. These

layered materials exhibit outstanding mechanical, electronic, magnetic and optical properties [35,38,44–57]. It was shown that in the Janus phases of these compounds, the breaking of the mirror symmetry brings Rashba-type spin-splitting [58–61] and that this, together with the large valley splitting, can give an important contribution to semiconductor valleytronics and spintronics. In the present work, the structural, electronic and magnetic properties of pristine VSi_2Z_4 (Z = P, As) and their Janus phase $VSiGeP_2As_2$ are explored. We found ferromagnetic ordering in these systems, and their magnetic anisotropy energy (MAE) reveals a strong dependency on the biaxial strain. In addition, an out-of-plane direction is found as an easy axis for the magnetization of VSi_2P_4, while an in-plane direction is favored in VSi_2As_4 and $VSiGeP_2As_2$. In the Janus phase, the compound presents breaking of the mirror symmetry. This can give piezoelectric properties, and is equivalent to having an electric field, which can manipulate magnetism and produce skyrmions in 2D materials [62,63]. Intriguingly, there occurs a topological phase transition from a trivial to topologically non-trivial state in $VSiGeP_2As_2$ monolayer, when the Hubbard U parameter is increased. Our investigation of these compounds opens prospects for studying their intrinsic magnetism, the interplay between magnetism and topology in two-dimensional materials and spin control in spintronics.

2. Computational Details

A first-principles relativistic approach based on density functional theory (DFT) using the Vienna Ab Initio Simulation Package (VASP) [64,65] is employed. The Perdew–Burke–Ernzerhof (PBE) formalism in the framework of generalized gradient approximation (GGA) is used to include the electron exchange-correlation [66]. Also, the projector-augmented wave scheme is implemented to resolve the Kohn-Sham equations through the plane-wave basis set. An energy cutoff of 500 eV is considered for the expansion of wave functions. The Monkhorst–Pack scheme is applied for *k*-point sampling with $15 \times 15 \times 1$ *k*-point mesh. The lattice constants were optimized at the PBE level. The optimized lattice constant for the Janus $VSiGeP_2As_2$ structure is 3.562 Å, which is between those of VSi_2P_4 (3.448 Å) and VSi_2As_4 (3.592 Å) monolayers. In addition, the convergence criterion for force is taken as 0.0001 eV/Å, while 10^{-7} eV of energy tolerance is considered for the lattice relaxation. Also, the number of electrons treated as valence is 41. In examining the dynamical stability, a $4 \times 4 \times 1$ supercell of $VSiGeP_2As_2$ monolayer is taken for calculating the phonon dispersion using the PHONOPY code [67]. The GGA + U routine, along with SOC, is executed, and the strongly correlated correction intended for V-*3d* is considered throughout the calculations. The values of the Hubbard parameter used for the d-orbitals of V are U = 4 eV for VSi_2P_4, and 2 eV for VSi_2As_4 and $VSiGeP_2As_2$, and the Hund coupling J_H is set at 0.87 eV. The main source of SOC in this compound is As; the value of SOC for As is estimated to be 0.164 eV [68,69].

3. Results and Discussion

The monolayered VSi_2Z_4 (Z = P, As) 2D materials crystallize in a hexagonal geometry with $P\bar{6}m2$ (No. 187) as the space group. These structures are seven-atom thick monolayered systems; the atoms are strongly bonded together with the order as Z-Si-Z-V-Z-Si-Z for pristine and P-Si-P-V-As-Ge-As in the case of the Janus phase. Figure 1a shows the pristine VSi_2P_4, VSi_2As_4 and Janus $VSiGeP_2As_2$ structures. The VSi_2Z_4 (Z = P, As) monolayers have broken inversion symmetry while protecting the mirror-plane symmetry with respect to V plane. In addition, the primitive cell with side and top views is shown for the Janus $VSiGeP_2As_2$ phase in Figure 1a, which presents the breaking of mirror symmetry with regard to the V atom. This is equivalent to an electric field, and the system can show piezoelectricity. The optimized lattice constants for VSi_2P_4 and VSi_2As_4 monolayers are 3.448 Å and 3.592 Å, respectively, whereas, for the Janus $VSiGeP_2As_2$ structure, it is 3.562 Å. Figure 1b presents the 2D Brillouin zone with the high-symmetry points indicated by red letters. Figure 1c shows the schematic representation for the topological transition as a function of onsite Coulomb interaction in $VSiGeP_2As_2$ monolayer.
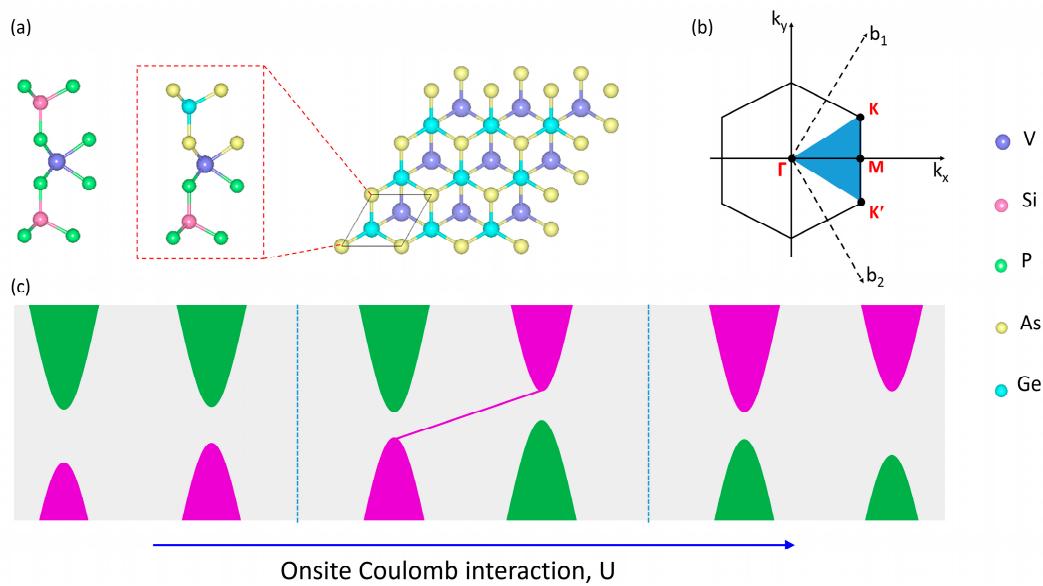
Figure 1. (**a**) Side view of VSi_2P_4 monolayer, side and top views for Janus phase $VSiGeP_2As_2$ primitive cell. (**b**) 2D Brillouin zone with the high-symmetry points indicated by red letters. (**c**) Schematic representation for the topological phase transition as a function of onsite Coulomb interaction observed in $VSiGeP_2As_2$ monolayer.

The stabilities of pristine VSi_2Z_4 (Z = P, As) monolayers and the Janus $VSiGeP_2As_2$ structure were studied through the cohesive energies and the phonon dispersion. The cohesive energies per atom (E_c) were computed; for VSi_2Z_4, $E_c = [E_{VSi2Z4} − (E_V + 2E_{Si} + 4E_Z)]/7$, where the energy terms E_{VSi2Z4}, E_V, E_{Si}, E_Z represent the total energies of the VSi_2Z_2 monolayer and that of V, Si and Z atoms, respectively. Similarly, for the Janus $VSiGeP_2As_2$, it can be written as $E_c = [E_{VSiGeP2As2} − (E_V + E_{Si} + E_{Ge} + 2E_P + 2E_{As})]/7$. The values of E_c were calculated as $−3.25$, $−2.60$ and $−2.92$ eV/atom for VSi_2P_4, VSi_2As_4 and $VSiGeP_2As_2$. These are relatively high compared to recently reported $MoSiGeP_2As_2$ ($−2.77$ eV/atom), $WGeSiP_2As_2$ ($−2.84$) [61] and other transition-metal based 2D Janus materials such as MoSSe, WSSe ($−2.34$ eV, $−2.06$ eV) [70]. Here, the phonon dispersion for $VSiGeP_2As_2$ is calculated along the high symmetry directions of the Brillouin zone (K-Γ-M-K) with the method of finite difference implemented in the Phonopy code. Figure 2a shows the phonon dispersion of $VSiGeP_2As_2$ revealing no imaginary frequency modes, thus dynamically stable. The pristine monolayers VSi_2Z_4 (Z = P, As) are already reported to be dynamically stable [9,31]. The large values of cohesive energies E_c, and the dynamical stability established from phononic spectra, can promise their experimental realization.

The electronic configuration for an unbonded V atom is $3d^34s^2$. However, the V atom in VSi_2Z_4 (Z = P, As) is trigonal-prismatically coordinated with six Z atoms. This type of crystal field divides the *3d* orbitals into dz^2, d_{yz}/d_{xz} and $d_{xy}/d_{x^2−y^2}$, as reported in MoS_2 for Mo atoms, which requires that dz^2 orbital should be occupied first [71]. The V atom donates four electrons to neighboring Z atoms, with one electron remaining, giving rise to V^{4+} valence state. With this one unpaired electron in dz^2, a magnetic moment of 1 μ_B is expected according to Hund's rule and the Pauli exclusion principle. Our DFT calculations indeed revealed a magnetic moment of ~1 μ_B per formula unit for VSi_2Z_4 (Z = P, As) and Janus $VSiGeP_2As_2$ structures. In addition, the total energies of two distinct magnetic configurations were evaluated in order to determine the magnetic ground state. For the antiferromagnetic (AFM) configuration, the magnetic moments were made antiparallel to nearest neighbors, while all of the magnetic moments were initialized in the same direction in the ferromagnetic (FM) configuration. In both instances, the spin orientations were off-plane. Figure 2b depicts these two common magnetic orderings with a $2 \times 2 \times 1$ supercell, for which the total energies and magnetic moments of the FM and AFM configurations were calculated, respectively. For the $2 \times 2 \times 1$ supercell, a magnetic moment of ~4.0 μ_B

is revealed for both the pristine and Janus phases in the FM state, while 0 μ_B is observed with the AFM alignment. Moreover, the energy difference between the FM and AFM states ($E_{FM} - E_{AFM}$) indicated negative energies, strongly suggesting intrinsic ferromagnetism in VSi_2Z_4 (Z = P, As) monolayers and their Janus structure. The optimized lattice constants a_o, the energy difference between the FM and AFM alignments and the easy axis for the magnetization for VSi_2Z_4 (Z = P, As) and Janus phase are reported in Table 1. We also computed the average electrostatic potential profiles along the *z*-axis for the pristine and the Janus phase. As indicated in Figure 2c,d, the profiles are symmetric for VSi_2Z_4 (Z = P, As). However, in the case of Janus $VSiGeP_2As_2$, the calculated average electrostatic potential is rather asymmetric with a work function difference, $\Delta\Phi$ of 0.35 eV (Figure 2e).
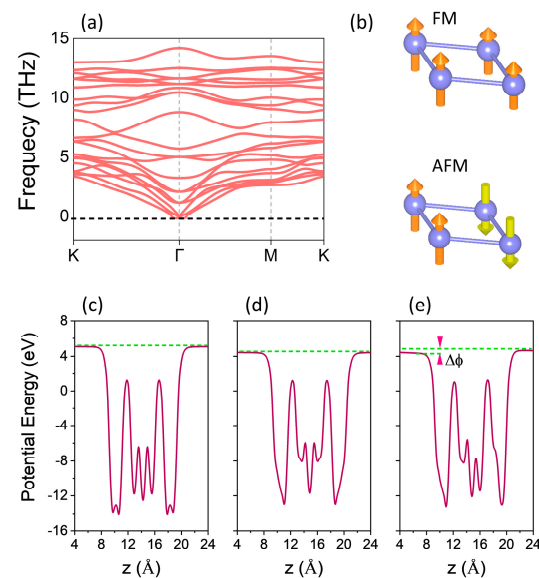

Figure 2. (**a**) The phonon dispersion for the Janus $VSiGeP_2As_2$ monolayer indicating no imaginary frequencies. (**b**) Two magnetic configurations FM and AFM, considered to evaluate the magnetic ground state. The planar average electrostatic potential energy of (**c**) VSi_2P_4, (**d**) VSi_2As_4, and (**e**) Janus $VSiGeP_2As_2$ monolayers. The work function difference $\Delta\Phi$ is estimated to be 0.35 eV for the Janus phase.

Table 1. Optimized lattice constants a_o, energy differences between the FM and AFM alignments and the easy axis for the magnetization.

Material	a_o (Å)	[$E_{FM} - E_{AFM}$] (eV)	Easy Axis
VSi_2P_4	3.448	−0.143	Out-of-plane
VSi_2As_4	3.592	−0.202	In-plane
$VSiGeP_2As_2$	3.562	−0.210	In-plane

The transition metal based 2D materials host degenerate energy valleys (at the K/K′ points of Brillouin zone) owing to a lack of inversion symmetry. Such energy valleys can be manipulated and utilized in valley-spin Hall effects and valley-spin locking [72–74]. Generating and controlling the valley polarization by making the K/K′ valleys non-degenerate is a big challenge in valleytronics. There are multiple means to lift this valley degeneracy between the K/K′ valleys and consequently generate the valley polarization. However, when an external magnetic field is removed, the polarization disappears. In general, the 2D monolayers preserve the long-range ferromagnetic ordering due to the intrinsic anisotropy. Specifically, in V-based TMDs, the spontaneous valley polarization results from the magnetic interaction among the V-3d electrons, which is independent of external fields and enables the modulation of spin and valley degrees of freedom. We therefore investigated the orbital-projected band structures of VSi_2Z_4 (Z = P, As) and Janus $VSiGeP_2As_2$ monolay-

ers, as shown in Figure 3. As illustrated, all three structures reveal nondegenerate energy values at the K and K′ valleys, and as a result they show different energy band gaps at the two valleys. The valley polarization is defined as [5], $\Delta E_{v/c} = E^{K'}_{v/c} - E^{K}_{v/c}$, where $E^{K,K'}_{v/c}$ represents the energies of electronic band edges at K/K′ valleys, correspondingly. In the case of VSi_2P_4, using this definition, we found a valley polarization of 76.6 meV in the bottom conduction band, while the top valence bands at K/K′ valleys remain almost degenerate with valley polarization of −3.9 meV. By contrast, for VSi_2As_4, the valley polarization is −8.2 meV in the bottom conduction band, whereas that of the top valence band is calculated to be ~88 meV. On the other hand, in the Janus phase, the bottom conduction bands at K/K′ remain almost degenerate in energy with valley polarization of −5 meV and 73.3 meV in the top valence bands. This reveals that intrinsic ferromagnetism is much more efficient in creating valley polarization. In addition, the conduction band minimum (CBM) in VSi_2P_4 is composed of V-d_{xy} and V-$d_{x^2-y^2}$ states at both K and K′ points, while the valence band maximum (VBM) is majorly composed of V-dz^2 orbitals. On the other hand, this orbital composition becomes reverse for pristine VSi_2As_4 and Janus $VSiGeP_2As_2$, i.e., V-dz^2 orbitals contribute to the CBM, while V-d_{xy} and V-$d_{x^2-y^2}$ form the VBM.
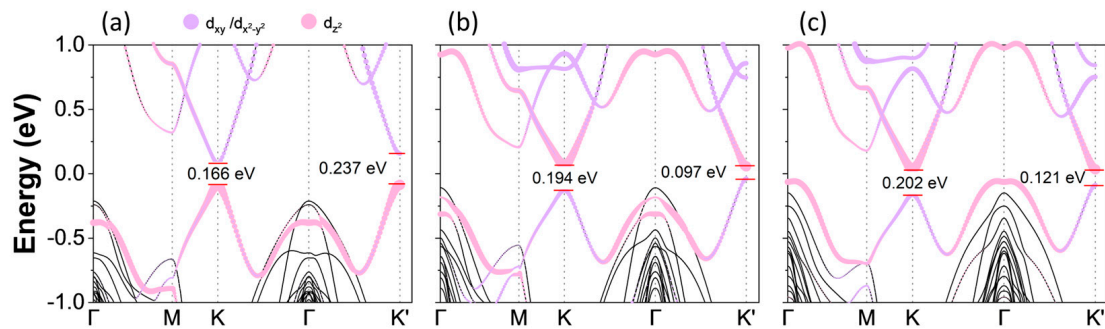
Figure 3. Orbitally resolved electronic band structures of (**a**) VSi_2P_4, (**b**) VSi_2As_4 and (**c**) $VSiGeP_2As_2$ Janus structure. The V-*3d* orbitals are represented by different colors, where the size of the colored dot describes the contribution from particular orbitals. The contribution decreases as the size of the colored dot decreases. The values of the Hubbard parameter used for the d-orbitals of V are U = 4 eV for VSi_2P_4, and 2 eV for VSi_2As_4 and $VSiGeP_2As_2$.

We studied the dependence of magnetic features of the VSi_2Z_4 and Janus $VSiGeP_2As_2$ on the biaxial strain. The energy difference between the FM and AFM configurations ($E_{FM} - E_{AFM}$), which determines the magnetic ground for the material, is illustrated in Figure 4 as a function of compressive and tensile strains. All systems retain the FM orderings under different biaxial strains and do not show any phase transition from FM to AFM state with the applied strain. The strain, in this instance, is defined as follows:

$$\varepsilon = \left(\frac{a - a_o}{a_o} \right) \times 100\%$$

Here, 'a_o' designates the lattice constant at a strainless state, and 'a' represents the strained lattice constant. The exchange parameter 'J', by taking into account the nearest neighbor exchange interactions, can be written as [28]:

$$J = -\left(\frac{E_{FM} - E_{AFM}}{6|\vec{S}|^2} \right)$$

where $|\vec{S}| = 1/2$, as the electronic configuration $3d^3 4s^2$ becomes $3d^1$ after losing four electrons. The energy differences between the FM and AFM alignments can be easily calculated using DFT ground state formalism, which can be used to compute the Heisenberg exchange

parameter 'J'. The large value of 'J', together with the magnetocrystalline anisotropy, will produce a large critical temperature.
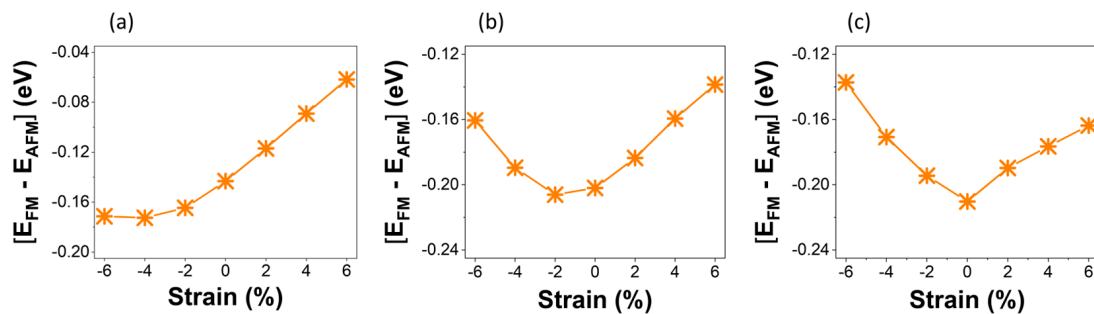

Figure 4. Strain dependence of energy differences between two magnetic configurations (FM and AFM) for (**a**) VSi_2P_4, (**b**) VSi_2As_4 and (**c**) $VSiGeP_2As_2$ Janus structures. The values of the Hubbard parameter used for the d-orbitals of V are U = 4 eV for VSi_2P_4, and 2 eV for VSi_2As_4 and $VSiGeP_2As_2$.

The magnetic anisotropy energy (MAE) is used to determine the easy axis for magnetization direction. It is defined as the energy difference between the out-of-plane and in-plane spin alignments, i.e., MAE = $E_\perp - E_{||}$. Consequently, a negative MAE will indicate an out-of-plane easy axis (perpendicular direction for magnetization), while positive values of MAE will indicate an in-plane easy axis (magnetization parallel to the plane direction). The MAE is originated because of the reliance of magnetic attributes on a specific crystallographic direction. Classically, dipole–dipole interactions are believed to be the origin of MAE, nonetheless quantum mechanically, the main cause lies in SOC [29]. For that reason, SOC effects should be considered in the evaluation of MAE. Thus, non-collinear calculations with SOC considered are carried out to evaluate the total energies ($E_\perp$, $E_{||}$) for the corresponding magnetization directions. We found MAE values of −4 μeV for VSi_2P_4 and 53 μeV in VSi_2As_4, indicating out-of-plane and in-plane magnetizations, respectively. Similarly, an in-plane magnetization is confirmed in $ViSiGeP_2As_2$ with an MAE value of 48 μeV. The direction of magnetization is essential to attain spontaneous valley polarization [14]. The effect of biaxial strain on MAE for all the monolayer systems is presented in Figure 5. One can see how the MAE is influenced by the tensile and compressive strains. For VSi_2P_4, the MAE decreases in either strain direction, with persistent out-of-plane easy axis for magnetization, as shown in Figure 5a. On the other hand, the in-plane easy axis in VSi_2As_4 is found tunable; it can be transformed to out-of-plane direction by applying some critical tensile or compressive strains, as indicated in Figure 5b. Likewise, an out-of-plane magnetization can be achieved in the Janus $ViSiGeP_2As_2$ monolayer at ε = 1.5%, as shown in Figure 5c. Shaded regions show the tuning of easy axis for the magnetization direction.
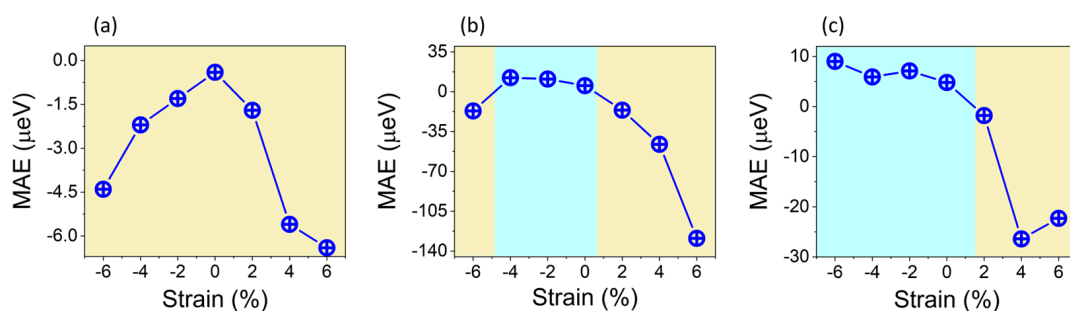

Figure 5. MAE as a function of biaxial strain calculated for two magnetic configurations ([001], [100]) (**a**) VSi_2P_4, (**b**) VSi_2As_4 and (**c**) $VSiGeP_2As_2$ Janus structures. Shaded regions indicate the modulation of the easy axis. The brown region is for an out-of-plane easy axis, while the cyan region indicates an in-plane easy axis. The values of the Hubbard parameter used for the d-orbitals of V are U = 4 eV for VSi_2P_4, and 2 eV for VSi_2As_4 and $VSiGeP_2As_2$.

Next, we show the electronic band structures of the Janus ViSiGeP$_2$As$_2$ monolayer by varying onsite Coulomb interaction known as the Hubbard parameter 'U', and by taking the SOC effect in consideration. Clearly, the CBM at the K/K$'$ valleys is made up of V-dz^2 orbitals when U = 2 eV is in the strain-free state, whereas the VBM is composed of V-d_{xy} and V-$d_{x^2-y^2}$ states. Upon increasing the Hubbard parameter 'U', the V-dz^2 orbitals come down in energy, while the $d_{xy}/d_{x^2-y^2}$ states go up in energy. When U reaches 2.8 eV, the system becomes gapless at the K$'$ point, although gapped at the K valley. The gapless nature of the band structure at K$'$ displays Weyl-like linear dispersion. Further raising U, the electronic band gap becomes smaller and smaller at the K valley. Conversely, at the K$'$ valley the band gap opens again with a band inversion exchanging the orbital contributions of the valence and conduction bands as compared to the band structure at U = 2 eV. Consequently, a topological phase transition occurs between U = 2.8 and U = 3.1 eV, leading to the emergence of the quantum anomalous Hall phase [5]. At U = 3.1 eV, the band gap closes at the K point and starts to reopen at 3.2 eV, with another band inversion achieved at the K valley. At U = 3.2 eV, we have a band inversion at both K and K$'$; as a result, the Janus structure is restored to the trivial ferrovalley insulating phase. The orbitally-projected band structure at U = 3.6 eV complies with all these behaviors. The evolution of band gaps and topological phases as a function of the electronic correlation at both K/K$'$ valleys is summarized in Figure 6h. As indicated, the trend of band gaps at the two valleys is quite similar; they begin to diminish, then reach zero, and finally they reopen by increasing U. As the band gap is smaller at K$'$ than at K valley (when U = 2 eV), the critical Hubbard parameter U necessary for closing the band gap is not similar; it is U = 2.8 eV and 3.1 eV, respectively. While usually the Coulomb repulsion kills the topological properties, in this case the Coulomb repulsion is necessary to observe the topological phase. Additionally, the range of U where the topological phase appears is between 2.8 and 3.1 eV, which is a realistic physical range for the Coulomb repulsion of 3d electrons. Moreover, the orbital characters at the K/K$'$ points of the Brillouin zone are investigated, as shown in schematic Figure 7, revealing the splitting of the energy levels of d orbitals in a trigonal prismatic crystal field environment. Here, only the middle layer containing V ions is displayed as the nonmagnetic top and bottom layers of these monolayers do not contribute to the spin density distribution.
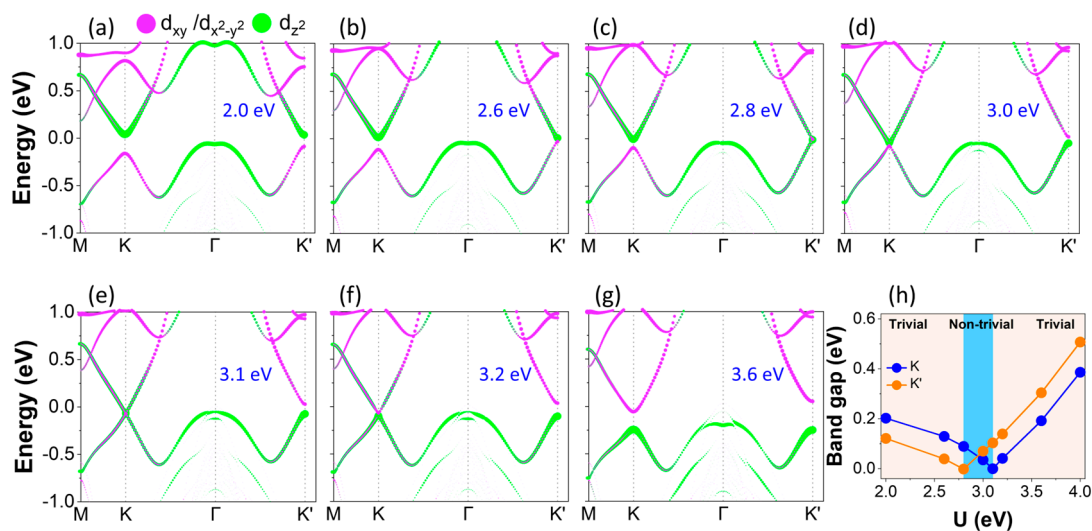
Figure 6. (**a–g**) Orbitally-resolved electronic band structures of the Janus VSiGeP$_2$As$_2$ monolayer with PBE + U and SOC included under different Hubbard parameter values U. The size of the colored dot is proportional to the weight of the corresponding orbitals. (**h**) Band gaps for the two K/K$'$ valleys.
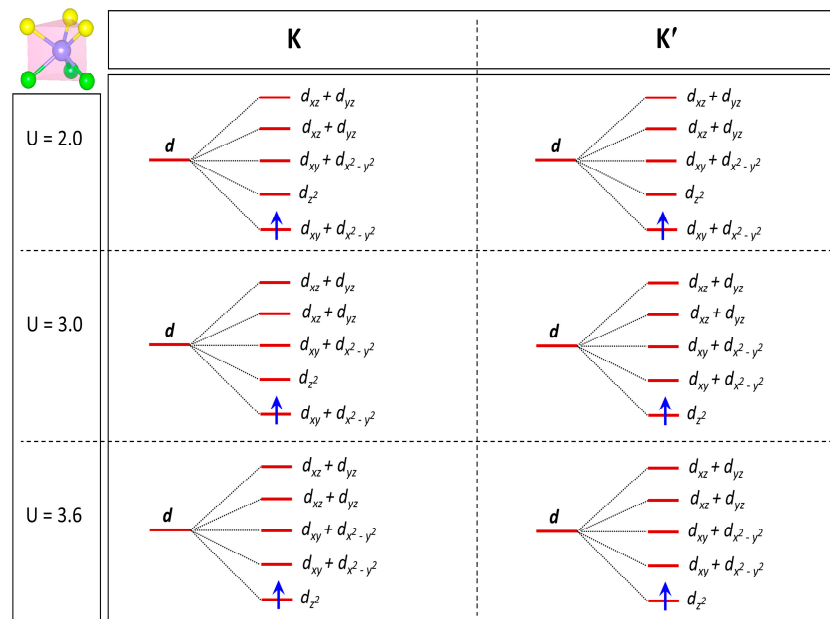
Figure 7. A schematic for the evolution of d orbitals of the spin up-subsector as a function of Hubbard parameter U for the Janus VSiGeP$_2$As$_2$ monolayer at K/K′ valleys. At U = 2 eV and U = 3.6 eV, the system is in the trivial ferrovalley insulating phase, while at U = 3 eV, it is in the topological phase.

4. Conclusions

In conclusion, based on first principles calculations, we present a detailed and comprehensive study of pristine VSi$_2$Z$_4$ (Z = P, As) and Janus VSiGeP$_2$As$_2$ monolayers. In the Janus phase, the compound shows breaking of the mirror symmetry, which is equivalent to having an electric field, and the system can be piezoelectric. After exploring their structural stability through ground state energies and phononic spectra, the electronic, magnetic and topological features were investigated. It was observed that these structures exhibit ground-state ferromagnetic ordering that persists at any tensile and compressive strains. In addition, VSi$_2$P$_4$ shows −4 μeV MAE with out-of-plane easy axis, which increases with the atomic number of pnictogens; for instance, in VSi$_2$As$_4$ the MAE increases dramatically to 53 μeV with in-plane magnetization direction. Likewise, an in-plane magnetization is established in VSiGeP$_2$As$_2$ with an MAE value of 48 μeV. In addition, we analyzed the effect of strain on the magnetic properties such as MAE, which revealed strong dependence on the biaxial strain.

We investigated how the topology of VSiGeP$_2$As$_2$ evolves as a function of the Coulomb interaction, and we observed the topological phase in the physical range of Hubbard U for 3d electrons. Our analysis of these emerging pristine and Janus-phased magnetic semiconductors opens prospects for studying the interplay between magnetism and topology in two-dimensional materials.

Author Contributions: Conceptualization, C.A., G.C., G.H.; Data curation, G.H.; Investigation, G.H.; Methodology, C.A., G.C., G.H.; Writing—original draft, C.A., G.C., G.H.; Writing—review editing, C.A., G.C., G.H., A.F., R.I., R.M.S.; supervision C.A., G.C. All authors have read and agreed to the published version of the manuscript.

Institutional Review Board Statement: Not applicable.

Informed Consent Statement: Not applicable.

References

1. Gong, C.; Li, L.; Li, Z.; Ji, H.; Stern, A.; Xia, Y.; Cao, T.; Bao, W.; Wang, C.; Wang, Y.; et al. Discovery of intrinsic ferromagnetism in two-dimensional van der Waals crystals. *Nature* **2017**, *546*, 265–269. [CrossRef] [PubMed]
2. Huang, B.; Clark, G.; Navarro-Moratalla, E.; Klein, D.R.; Cheng, R.; Seyler, K.L.; Zhong, D.; Schmidgall, E.; McGuire, M.A.; Cobden, D.H.; et al. Layer-dependent ferromagnetism in a van der Waals crystal down to the monolayer limit. *Nature* **2017**, *546*, 270–273. [CrossRef] [PubMed]
3. Li, Y.; Legut, D.; Liu, X.; Lin, C.; Feng, X.; Li, Z.; Zhang, Q. Modulated Ferromagnetism and Electric Polarization Induced by Surface Vacancy in MX_2 Monolayers. *J. Phys. Chem. C* **2022**, *126*, 8817–8825. [CrossRef]
4. Tiwari, S.; Vanherck, J.; Van de Put, M.L.; Vandenberghe, W.G.; Sorée, B. Computing Curie temperature of two-dimensional ferromagnets in the presence of exchange anisotropy. *Phys. Rev. Res.* **2021**, *3*, 043024. [CrossRef]
5. Sheng, K.; Zhang, B.; Yuan, H.-K.; Wang, Z.-Y. Strain-engineered topological phase transitions in ferrovalley $2H-RuCl_2$ monolayer. *Phys. Rev. B* **2022**, *105*, 195312. [CrossRef]
6. Li, C.; An, Y. Tunable magnetocrystalline anisotropy and valley polarization in an intrinsic ferromagnetic Janus $2H$-VTeSe monolayer. *Phys. Rev. B* **2022**, *106*, 115417. [CrossRef]
7. Yin, Y.; Gong, Q.; Yi, M.; Guo, W. Emerging versatile two-dimensional $MoSi_2N_4$ family. *arXiv* **2022**, arXiv:2211.00827.
8. Islam, R.; Ghosh, B.; Autieri, C.; Chowdhury, S.; Bansil, A.; Agarwal, A.; Singh, B. Tunable spin polarization and electronic structure of bottom-up synthesized $MoSi_2N_4$ materials. *Phys. Rev. B* **2021**, *104*, L201112. [CrossRef]
9. Feng, X.; Xu, X.; He, Z.; Peng, R.; Dai, Y.; Huang, B.; Ma, Y. Valley-related multiple Hall effect in monolayer VSi_2P_4. *Phys. Rev. B* **2021**, *104*, 075421. [CrossRef]
10. Autieri, C.; Cuono, G.; Noce, C.; Rybak, M.; Kotur, K.M.; Agrapidis, C.E.; Wohlfeld, K.; Birowska, M. Limited Ferromagnetic Interactions in Monolayers of MPS_3 (M = Mn and Ni). *J. Phys. Chem. C* **2022**, *126*, 6791–6802. [CrossRef]
11. Basnet, R.; Kotur, K.M.; Rybak, M.; Stephenson, C.; Bishop, S.; Autieri, C.; Birowska, M.; Hu, J. Controlling magnetic exchange and anisotropy by non-magnetic ligand substitution in layered MPX_3 (M = Ni, Mn; X = S, Se). *Phys. Rev. Res.* **2022**, *4*, 023256. [CrossRef]
12. Liu, W.; Guo, X.; Schwartz, J.; Xie, H.; Dhale, N.U.; Sung, S.H.; Kondusamy, A.L.N.; Wang, X.; Zhao, H.; Berman, D. A three-stage magnetic phase transition revealed in ultrahigh-quality van der Waals bulk magnet CrSBr. *ACS Nano* **2022**, *16*, 15917–15926. [CrossRef] [PubMed]
13. Liu, X.; Taddei, K.M.; Li, S.; Liu, W.; Dhale, N.; Kadado, R.; Berman, D.; Cruz, C.D.; Lv, B. Canted antiferromagnetism in the quasi-one-dimensional iron chalcogenide $BaFe_2Se_4$. *Phys. Rev. B* **2020**, *102*, 180403. [CrossRef]
14. Liu, P.; Liu, S.; Jia, M.; Yin, H.; Zhang, G.; Rena, F.; Wanga, B.; Liu, C. Strain-driven valley states and phase transitions in Janus $VSiGeN_4$ monolayer. *Appl. Phys. Lett.* **2022**, *121*, 063103. [CrossRef]
15. Deng, Y.; Yu, Y.; Song, Y.; Zhang, J.; Wang, N.Z.; Sun, Z.; Yi, Y.; Wu, Y.Z.; Zhu, J. Gate-tunable room-temperature ferromagnetism in two-dimensional Fe_3GeTe_2. *Nature* **2018**, *563*, 94–99. [CrossRef] [PubMed]
16. Gibertini, M.; Koperski, M.; Morpurgo, A.F.; Novoselov, K.S. Magnetic 2D materials and heterostructures. *Nat. Nanotechnol.* **2019**, *14*, 408–419. [CrossRef]
17. Huang, B.; Clark, G.; Klein, D.; MacNeill, D.; Navarro-Moratalla, E.; Seyler, K.; Wilson, N.; McGuire, M.; Cobden, D.; Xiao, D. Electrical control of 2D magnetism in bilayer CrI_3. *Nat. Nanotechnol.* **2018**, *13*, 544–548. [CrossRef]
18. Burch, K.S. Electric switching of magnetism in 2D. *Nat. Nanotechnol.* **2018**, *13*, 532. [CrossRef]
19. Tian, Y.; Gao, W.; Henriksen, E.A.; Chelikowsky, J.R.; Yang, L. Optically driven magnetic phase transition of monolayer $RuCl_3$. *Nano Lett.* **2019**, *19*, 7673–7680. [CrossRef]
20. Zhao, Y.; Lin, L.; Zhou, Q.; Li, Y.; Yuan, S.; Chen, Q.; Dong, S.; Wang, J. Surface vacancy-induced switchable electric polarization and enhanced ferromagnetism in monolayer metal trihalides. *Nano Lett.* **2018**, *18*, 2943–2949. [CrossRef]
21. Song, X.; Yuan, F.; Schoop, L.M. The properties and prospects of chemically exfoliated nanosheets for quantum materials in two dimensions. *Appl. Phys. Rev.* **2021**, *8*, 011312. [CrossRef]
22. Jiang, S.; Xie, H.; Shan, J.; Mak, K.F. Exchange magnetostriction in two-dimensional antiferromagnets. *Nat. Mater.* **2020**, *19*, 1295–1299. [CrossRef] [PubMed]

23. Mermin, N.D.; Wagner, H. Absence of ferromagnetism or antiferromagnetism in one-or two-dimensional isotropic Heisenberg models. *Phys. Rev. Lett.* **1966**, *17*, 1133. [CrossRef]

24. Lado, J.L.; Fernández-Rossier, J. On the origin of magnetic anisotropy in two dimensional CrI_3. *2D Mater.* **2017**, *4*, 035002. [CrossRef]

25. Gurney, B.; Yamada, K.; Nakatani, Y.; Prejbeanu, I.-L.; Diény, B.; Pirro, P.; Hillebrands, B. Spin valve giant magnetoresistive sensor materials for hard disk drives. In *Ultrathin Magnetic Structures IV*; Springer: Berlin/Heidelberg, Germany, 2005; pp. 149–175.

26. Prinz, G.A. Magnetoelectronics. *Science* **1998**, *282*, 1660–1663. [CrossRef]

27. Kryder, M.H. Magnetic thin films for data storage. *Thin Solid Films* **1992**, *216*, 174–180. [CrossRef]

28. Webster, L.; Yan, J.-A. Strain-tunable magnetic anisotropy in monolayer $CrCl_3$, $CrBr_3$, and CrI_3. *Phys. Rev. B* **2018**, *98*, 144411. [CrossRef]

29. Singla, R.; Hackett, T.A.; Kumar, S.; Sharmad, J.; Kashyap, M.K. Curie temperature engineering in a novel 2D analog of iron ore (hematene) via strain. *Nanoscale Adv.* **2020**, *2*, 5890–5896. [CrossRef]

30. Hussain, G.; Manzoor, M.; Iqbal, M.W.; Muhammad, I.; Bafekry, A.; Ullah, H.; Autieri, C. Strain modulated electronic and optical properties of laterally stitched $MoSi_2N_4/XSi_2N_4$ (X = W, Ti) 2D heterostructures. *Phys. E Low-Dimens. Syst. Nanostruct.* **2022**, *144*, 115471. [CrossRef]

31. Zhang, J.; Wang, Y.; Hua, C.; Yang, S.; Liu, Y.; Luo, J.; Liu, T.; Nai, J.; Tao, X. Prediction of bipolar VSi_2As_4 and VGe_2As_4 monolayers with high Curie temperature and strong magnetocrystalline anisotropy. *Phys. Rev. B* **2022**, *106*, 235401. [CrossRef]

32. Hussain, G.; Cuono, G.; Islam, R.; Trajnerowicz, A.; Jureńczyk, J.; Autieri, C.; Dietl, T. Electronic and optical properties of $InAs/InAs_{0.625}Sb_{0.375}$ superlattices and their application for far-infrared detectors. *J. Phys. D Appl. Phys.* **2022**, *55*, 495301. [CrossRef]

33. Dey, D.; Ray, A.; Yu, L. Intrinsic ferromagnetism and restrictive thermodynamic stability in MA_2N_4 and Janus $VSiGeN_4$ monolayers. *Phys. Rev. Mater.* **2022**, *6*, L061002. [CrossRef]

34. Hong, Y.-L.; Liu, Z.; Wang, L.; Zhou, T.; Ma, W.; Xu, C.; Feng, S.; Chen, L.; Chen, M.-L.; Sun, D.-M. Chemical vapor deposition of layered two-dimensional $MoSi_2N_4$ materials. *Science* **2020**, *369*, 670–674. [CrossRef] [PubMed]

35. Cao, L. Two-dimensional van der Waals electrical contact to monolayer $MoSi_2N_4$. *Appl. Phys. Lett.* **2021**, *118*, 013106. [CrossRef]

36. Bafekry, A.; Faraji, M.; Hoat, D.M.; Shahrokhi, M.; Fadlallah, M.M.; Feghhi, S.A.H.; Ghergherehchi, M.; Gogova, D. $MoSi_2N_4$ single-layer: A novel two-dimensional material with outstanding mechanical, thermal, electronic and optical properties. *J. Phys. D Appl. Phys.* **2021**, *54*, 155303. [CrossRef]

37. Mortazavi, B.; Javvaji, B.; Shojaei, F.; Rabczuk, T.; Shapeev, A.V.; Zhuang, X. Exceptional piezoelectricity, high thermal conductivity and stiffness and promising photocatalysis in two-dimensional $MoSi_2N_4$ family confirmed by first-principles. *Nano Energy* **2021**, *82*, 105716. [CrossRef]

38. Jian, C.-C.; Ma, X.; Zhang, J.; Yong, X. Strained $MoSi_2N_4$ monolayers with excellent solar energy absorption and carrier transport properties. *J. Phys. Chem. C* **2021**, *125*, 15185–15193. [CrossRef]

39. Wang, Q.; Cao, L.; Liang, S.-J.; Wu, W.; Wang, G.; Lee, C.H.; Ong, W.L.; Yang, H.Y.; Ang, L.K.; Yang, S.A.; et al. Efficient Ohmic contacts and built-in atomic sublayer protection in $MoSi_2N_4$ and WSi_2N_4 monolayers. *npj 2D Mater. Appl.* **2021**, *5*, 71. [CrossRef]

40. Yu, J.; Zhou, J.; Wan, X.; Li, Q. High intrinsic lattice thermal conductivity in monolayer $MoSi_2N_4$. *New J. Phys.* **2021**, *23*, 033005. [CrossRef]

41. Cui, Z.; Luo, Y.; Yu, J.; Xu, Y. Tuning the electronic properties of $MoSi_2N_4$ by molecular doping: A first principles investigation. *Phys. E Low-Dimens. Syst. Nanostruct.* **2021**, *134*, 114873. [CrossRef]

42. Bafekry, A.; Faraji, M.; Fadlallah, M.M.; Khatibani, A.B.; Ziabari, A.; Ghergherehchi, M.; Nedaei, S.; Shayesteh, S.F.; Gogova, D. Tunable electronic and magnetic properties of $MoSi_2N_4$ monolayer via vacancy defects, atomic adsorption and atomic doping. *Appl. Surf. Sci.* **2021**, *559*, 149862. [CrossRef]

43. Yao, H.; Zhang, C.; Wang, Q.; Li, J.; Yu, Y.; Xu, F.; Wang, B.; Wei, Y. Novel Two-Dimensional Layered $MoSi_2Z_4$ (Z = P, As): New Promising Optoelectronic Materials. *Nanomaterials* **2021**, *11*, 559. [CrossRef] [PubMed]

44. Lv, X.; Xu, Y.; Mao, B.; Liu, G.; Zhao, G.; Yang, J. Strain modulation of electronic and optical properties of monolayer $MoSi_2N_4$. *Phys. E Low-Dimens. Syst. Nanostruct.* **2022**, *135*, 114964. [CrossRef]

45. Pham, D. Electronic properties of a two-dimensional van der Waals $MoGe_2N_4/MoSi_2N_4$ heterobilayer: Effect of the insertion of a graphene layer and interlayer coupling. *RSC Adv.* **2021**, *11*, 28659–28666. [CrossRef]

46. Yuan, G.; Cheng, Z.; Cheng, Y.; Hui, W.D.; Liu, Z.; Han, C.; Ma, X. Highly Sensitive Band Alignment of Graphene/$MoSi_2N_4$ Heterojunction via External Electric Field. *ACS Appl. Electron. Mater.* **2022**, *4*, 2897–2905. [CrossRef]

47. Chen, R.; Chen, D.; Zhang, W. First-principles calculations to investigate stability, electronic and optical properties of fluorinated $MoSi_2N_4$ monolayer. *Results Phys.* **2021**, *30*, 104864. [CrossRef]

48. Bafekry, A.; Faraji, M.; Stampfl, C.; Sarsari, A.; Ziabari, A.; Hieu, N.N.; Karbasizadeh, S.; Ghergherehchi, M. Band-gap engineering, magnetic behavior and Dirac-semimetal character in the $MoSi_2N_4$ nanoribbon with armchair and zigzag edges. *J. Phys. D Appl. Phys.* **2021**, *55*, 035301. [CrossRef]

49. Ray, A.; Tyagi, S.; Singh, N.; Schwingenschlögl, U. Inducing Half-Metallicity in Monolayer $MoSi_2N_4$. *ACS Omega* **2021**, *6*, 30371–30375. [CrossRef]

50. Ng, J.Q.; Wu, Q.; Ang, L.K.; Ang, Y.S. Tunable electronic properties and band alignments of $MoSi_2N_4/GaN$ and $MoSi_2N_4/ZnO$ van der Waals heterostructures. *Appl. Phys. Lett.* **2022**, *120*, 103101. [CrossRef]

51. Xu, J.; Wu, Q.; Sun, Z.; Mwankemwa, N.; Zhang, W.-b.; Yang, W.-x. First-principles investigations of electronic, optical, and photocatalytic properties of Au-adsorbed MoSi$_2$N$_4$ monolayer. *J. Phys. Chem. Solids* **2022**, *162*, 110494. [CrossRef]
52. Bafekry, A.; Stampfl, C.; Naseri, M.; Fadlallah, M.M.; Faraji, M.; Ghergherehchi, M.; Gogova, D.; Feghhi, S.A.H. Effect of electric field and vertical strain on the electro-optical properties of the MoSi$_2$N$_4$ bilayer: A first-principles calculation. *J. Appl. Phys.* **2021**, *129*, 155103. [CrossRef]
53. Li, Q.; Zhou, W.; Wan, X.; Zhou, J. Strain effects on monolayer MoSi$_2$N$_4$: Ideal strength and failure mechanism. *Phys. E Low-Dimens. Syst. Nanostruct.* **2021**, *131*, 114753. [CrossRef]
54. Hussain, G.; Asghar, M.; Iqbal, M.W.; Ullah, H.; Autieri, C. Exploring the structural stability, electronic and thermal attributes of synthetic 2D materials and their heterostructures. *Appl. Surf. Sci.* **2022**, *590*, 153131. [CrossRef]
55. Islam, R.; Hussain, G.; Verma, R.; Talezadehlari, M.S.; Muhammad, Z.; Singh, B.; Autieri, C. Fast electrically switchable large gap quantum spin Hall states in MGe$_2$Z$_4$. *arXiv* **2022**, arXiv:2211.06443.
56. Sheoran, S.; Monga, S.; Phutela, A.; Bhattacharya, S. Coupled Spin-Valley, Rashba Effect, and Hidden Spin Polarization in WSi$_2$N$_4$ Family. *J. Phys. Chem. Lett.* **2023**, *14*, 1494–1503. [CrossRef]
57. Islam, R.; Verma, R.; Ghosh, B.; Muhammad, Z.; Bansil, A.; Autieri, C.; Singh, B. Switchable large-gap quantum spin Hall state in the two-dimensional MSi$_2$Z$_4$ class of materials. *Phys. Rev. B* **2022**, *106*, 245149. [CrossRef]
58. Van Thiel, T.; Brzezicki, W.; Autieri, C.; Hortensius, R.; Afanasiev, D.; Gauquelin, N.; Jannis, D.; Janssen, N.; Groenendijk, J.; Fatermans, J.; et al. Coupling charge and topological reconstructions at polar oxide interfaces. *Phys. Rev. Lett.* **2021**, *127*, 127202. [CrossRef]
59. Smaili, I.; Laref, S.; Garcia, J.H.; Schwingenschlögl, U.; Roche, S.; Manchon, A. Janus monolayers of magnetic transition metal dichalcogenides as an all-in-one platform for spin-orbit torque. *Phys. Rev. B* **2021**, *104*, 104415. [CrossRef]
60. Zhao, X.; Wang, Z.; Chen, J.; Wang, B. Topological properties of Xene turned by perpendicular electric field and exchange field in the presence of Rashba spin-orbit coupling. *J. Phys. Condens. Matter* **2022**, *35*, 095401. [CrossRef]
61. Hussain, G.; Samad, A.; Rehman, M.U.; Cuono, G.; Autieri, C. Emergence of Rashba splitting and spin-valley properties in Janus MoGeSiP$_2$As$_2$ and WGeSiP$_2$As$_2$ monolayers. *J. Magn. Magn. Mater.* **2022**, *563*, 169897. [CrossRef]
62. Dou, K.; Du, W.; He, Z.; Dai, Y.; Huang, B.; Ma, Y. Theoretical Prediction of Antiferromagnetic Skyrmion Crystal in Janus Monolayer CrSi$_2$N$_2$As$_2$. *ACS Nano* **2023**, *17*, 1144–1152. [CrossRef] [PubMed]
63. Laref, S.; Goli, V.M.L.D.P.; Smaili, I.; Schwingenschlögl, U.; Manchon, A. Topologically stable bimerons and skyrmions in vanadium dichalcogenide Janus monolayers. *arXiv* **2020**, arXiv:2011.07813.
64. Kresse, G.; Joubert, D. From ultrasoft pseudopotentials to the projector augmented-wave method. *Phys. Rev. B* **1999**, *59*, 1758. [CrossRef]
65. Kresse, G.; Furthmüller, J. Efficient iterative schemes for ab initio total-energy calculations using a plane-wave basis set. *Phys. Rev. B* **1996**, *54*, 11169. [CrossRef] [PubMed]
66. Perdew, J.P.; Burke, K.; Ernzerhof, M. Generalized gradient approximation made simple. *Phys. Rev. Lett.* **1996**, *77*, 3865. [CrossRef] [PubMed]
67. Togo, A.; Tanaka, I. First principles phonon calculations in materials science. *Scr. Mater.* **2015**, *108*, 1–5. [CrossRef]
68. Cuono, G.; Autieri, C.; Guarnaccia, G.; Avella, A.; Cuoco, M.; Forte, F.; Noce, C. Spin–orbit coupling effects on the electronic properties of the pressure-induced superconductor CrAs. *Eur. Phys. J. Spec. Top.* **2019**, *228*, 631–641. [CrossRef]
69. Wadge, A.S.; Grabecki, G.; Autieri, C.; Kowalski, B.J.; Iwanowski, P.; Cuono, G.; Islam, M.F.; Canali, C.M.; Dybko, K.; Hruban, A.; et al. Electronic properties of TaAs$_2$ topological semimetal investigated by transport and ARPES. *J. Phys. Condens. Matter* **2022**, *34*, 125601. [CrossRef]
70. Li, F.; Wei, W.; Zhao, P.; Huang, B.; Dai, Y. Electronic and optical properties of pristine and vertical and lateral heterostructures of Janus MoSSe and WSSe. *J. Phys. Chem. Lett.* **2017**, *8*, 5959–5965. [CrossRef]
71. Yan, S.; Qiao, W.; He, X.; Guo, X.; Xi, L.; Zhong, W.; Du, Y. Enhancement of magnetism by structural phase transition in MoS$_2$. *Appl. Phys. Lett.* **2015**, *106*, 012408. [CrossRef]
72. Ominato, Y.; Fujimoto, J.; Matsuo, M. Valley-dependent spin transport in monolayer transition-metal dichalcogenides. *Phys. Rev. Lett.* **2020**, *124*, 166803. [CrossRef] [PubMed]
73. Ahammed, R.; De Sarkar, A. Valley spin polarization in two-dimensional $h-M$N (M = Nb, Ta) monolayers: Merger of valleytronics with spintronics. *Phys. Rev. B* **2022**, *105*, 045426. [CrossRef]
74. Cui, Q.; Zhu, Y.; Liang, J.; Cui, P.; Yang, H. Spin-valley coupling in a two-dimensional VSi$_2$N$_4$ monolayer. *Phys. Rev. B* **2021**, *103*, 085421. [CrossRef]